Estimation of rock physics properties via FWI of VSP data recorded by accelerometer and fiberoptic sensors

Qi Hu, Matt Eaid, Scott Keating, and Kristopher A. Innanen, and Xiaohui Cai

ABSTRACT

Combining elastic full waveform inversion (FWI) with rock physics can extend the role of FWI from seismic imaging to quantitative prediction and monitoring of reservoir parameters. Distributed Acoustic Sensing (DAS), a rapidly developing seismic acquisition technology, has the potential to be an enabler for such applications of FWI. In this study, we apply a sequential inversion scheme combining elastic FWI and Bayesian rock physics inversion to a vertical seismic profile (VSP) dataset acquired with accelerometers and collocated distributed acoustic sensing (DAS) fiber at the Carbon Management Canada's Newell County Facility. The goal is to build a baseline model of porosity and lithology parameters to support later monitoring of CO_2 storage. Our key strategies include an effective source approach to cope with near-surface complications, a modeling strategy to simulate DAS data directly comparable to the field data, and a Gaussian mixture approach to capture the bimodality of rock properties. We perform FWI tests on the accelerometer, DAS, and combined accelerometer-DAS data. While our inversion results can accurately reproduce either type of data, the elastic models inverted from the accelerometer data outperform the other two in matching well logs and identifying the target reservoir. We attribute this result to the insignificant advantage of DAS data, in this case, over accelerometer data, which also suffers from single-component measurements and lower signal-to-noise ratios. The porosity and lithology models predicted from the accelerometer elastic models are reasonably accurate at the well location and are geologically meaningful in spatial distribution.

INTRODUCTION

The Carbon Management Canada's (CMC) Newell County Facility is a platform for development and performance validation of technologies intended for measurement, monitoring and verification of CO_2 storage (Lawton et al., 2019; Macquet et al., 2022). In 2018, a vertical seismic profile (VSP) survey was acquired using accelerometers and collocated distributed acoustic sensing (DAS) fiber in an observation well at the field site (Hall et al., 2019). One of the goals of this survey was to obtain a baseline data set to compare against later monitoring data, gathered during the course of CO_2 storage. In this study, we propose a workflow combining full waveform inversion (FWI) and rock physics to predict reservoir properties from the measured data, to develop the pre-injection baseline model.

A combination of seismic inversion for elastic properties (e.g., velocity, density, and modulus) and rock physics for predicting reservoir properties (e.g., porosity, lithology, and fluid saturation) is a classical procedure in reservoir characterization (Doyen, 2007; Dvorkin et al., 2014; Grana et al., 2021). The seismic inversion is generally performed using the convolutional model based on a linearized approximation of the Zoeppritz equations (Aki and Richards, 2002; Buland and Omre, 2003). This approach is simple to implement and computationally fast. FWI methods, although computationally challenging, have the capacity to produce a more accurate elastic model by involving a more complete subset of

the information content of seismic data (Tarantola, 1986; Brossier et al., 2009; Virieux and Operto, 2009; Mallick and Adhikari, 2015; Pan et al., 2018; Hu et al., 2021). Therefore, FWI appears to be a potentially powerful tool for reservoir characterization. The prediction of reservoir properties from elastic attributes requires a rock physics model (Mavko et al., 2020). The model adopted in the inversion depends on the geological environment and must be calibrated using well logs or laboratory measurements of core samples. The rock physics inversion is often formulated in a Bayesian framework, allowing uncertainty in the model predictions to be assessed through a probability density function (Bosch et al., 2010). Under some restrictive assumptions (Grana et al., 2021), we can derive a closed-form solution of this problem, thus significantly reducing the computational cost. In CO_2 storage applications, progress has been reported in combining FWI and rock physics for predicting the time evolution of CO_2 saturation (Queißer and Singh, 2013; Dupuy et al., 2016, 2021; Hu et al., 2023). In these studies, the recovered baseline model of reservoir properties, such as porosity and lithology, help to reduce the uncertainty in fluid predictions of the monitor stage.

Since the estimates of elastic parameters directly affect the result of rock physics interpretation, obtaining an accurate FWI model is the key to using FWI for reservoir characterization. At the land-based Newell County Facility, one of the challenges FWI faces is the near-surface heterogeneity. The unconsolidated nature of the sediment in proximity to Earth's surface leads to complex seismic wave propagation that is heavily influenced by surface waves, attenuation and dispersion, and spatially varying source signatures. Additionally, there is limited prior information about the near surface that can be used to constrain the inversion. As a result, FWI may fail to converge because of the difficulties that exist in accurately characterizing the near surface and the significant impact it has on seismic data. Efforts have been made to use surface wave based approaches for near-surface velocity estimation (Dokter et al., 2017; Köhn et al., 2019; Borisov et al., 2020; Colombo et al., 2021; Pan et al., 2023). In the absence of robust near-surface information, Keating et al. (2021) proposed an effective source approach for VSP FWI. The idea is to remove the near surface from inversion by introducing an unknown a variable characterizing the wavefield at depth that best explains the data. This approach does not require a complete understanding of surface source signatures.

Another challenge for FWI is the incomplete nature of the data we record. Due to limitations on the acquisition geometry and seismic bandwidth, multiparameter FWI of land data is a difficult proposition (Brossier et al., 2009; Plessix et al., 2013; Stopin et al., 2014). The advent of DAS, an acquisition technology that employs optical fibers to sense seismically induced strain (Posey Jr et al., 2000), supplies an additional subset of the data that could contain the information required to propel FWI forward (Egorov et al., 2018; Eaid et al., 2020; Pan et al., 2023). In fact, the conventional point sensors (e.g., 3C geophone) directly measure multiple elastic wavefield components, and do so with a relatively high signal-to-noise ratio (SNR), but are limited in the low-frequencies they can sense and where they can be cost-effectively deployed; DAS senses low-frequencies effectively (Becker et al., 2017; Jin and Roy, 2017), and can occupy boreholes without disturbing production processes (Mateeva et al., 2014; Harris et al., 2016; Byerley et al., 2018), but have a generally lower SNR and are fundamentally single-component (Kuvshinov, 2016). The two sensor types can be viewed as supplying complementary datasets, which may lead to

improved inversion results.

A previous FWI study for the 2018 VSP survey is provided by Eaid et al. (2023). Two of the strategies proposed in their study include an effective source approach to address near-surface complexity and a single-term parameterization approach to reduce the ill-posedness of the FWI problem. This single parameter is related to the trendline in the coordinate space of P-wave velocity, S-wave velocity, and density, obtained by regression of well-log data. While using this parameterization offers advantages, it introduces inherent errors to the inversion by assuming a perfect correlation between velocity and density, and also causes a loss of elasticity information in the result that is important for reservoir property characterization. This study extends the analysis of Eaid et al. (2023) for the target area to three-parameter elastic inversion and rock physics interpretation, and the main purpose is to explore the potential of FWI in quantitative seismic reservoir characterization.

The paper is organized as follows. First, we present the FWI framework used throughout this study. We show how to convert a conventional FWI scheme into a simultaneous inversion for source wavefields and elastic models. We also describe the modeling strategies that can simulate DAS data that is directly comparable to the field data. Then, we describe the Bayesian approach we use to predict rock physics properties from FWI results. In the section of field data application, we first give a brief introduction to the VSP experiment at the CMC Newell County Facility. We then describe the preparations before inversion, including seismic data processing and rock physics analysis of well-log data. Finally, we apply a sequential inversion scheme combing FWI and rock physics to the processed data, including both accelerometer and DAS measurements.

METHODS

Frequency-domain elastic FWI

The FWI problem can be framed as an attempt to minimize the mismatch between data and model predictions, subject to a wave propagation model linking the wavefield and subsurface together (Métivier et al., 2017). The inverse problem can be stated as

$$\min_{\mathbf{m}} E = \frac{1}{2}\sum_{i=1}^{N_s}\sum_{j=1}^{N_\omega} \|\mathbf{R}\mathbf{u}_{i,j} - \mathbf{d}_{i,j}\|_2^2 \quad \text{subject to} \quad \mathbf{A}(\omega,\mathbf{m})\mathbf{u} = \mathbf{f}(\omega), \tag{1}$$

where E is the objective function, $\mathbf{d}$ is the observed data, $\mathbf{R}$ is a sampling matrix representing receiver measurement, and N_s and N_ω are the number of sources and the number of frequencies, respectively. Here we consider the 2D frequency-domain isotropic-elastic wave equation (Pratt, 1990): $\mathbf{A}$ is the finite-difference forward operator dependent on the modeled frequency ω and the medium properties $\mathbf{m}$, $\mathbf{u}$ is the displacement wavefield, and $\mathbf{f}$ is the source term. In the following discussion, we will not explicitly state the sums over sources and frequencies for simplicity.

According to the adjoint state method (Plessix, 2006), the Lagrangian of the minimization problem in eq. (1) is

$$L(\mathbf{m},\mathbf{u},\lambda) = \frac{1}{2}\|\mathbf{R}\mathbf{u} - \mathbf{d}\|_2^2 + \Re\langle \mathbf{A}\mathbf{u} - \mathbf{f}, \lambda\rangle, \tag{2}$$

where λ is the Lagrange multiplier, $\Re$ indicates the real part, and $\langle ., . \rangle$ is the scalar product, e.g., for two complex matrices, $\mathbf{a}$ and $\mathbf{b}$, of the size N, $\langle \mathbf{a}, \mathbf{b} \rangle = \sum_{i=1}^{N} \mathbf{a}_i^* \mathbf{b}_i$, where the superscript * represents the complex conjugate. Let $\overline{\mathbf{u}}$ denotes the solution of the wave equation, such that $\mathbf{A}\overline{\mathbf{u}} = \mathbf{f}$, we have

$$L(\mathbf{m}, \overline{\mathbf{u}}, \lambda) = E, \tag{3}$$

and the gradient of E yields

$$\nabla_{\mathbf{m}} E = \frac{dL(\mathbf{m}, \overline{\mathbf{u}}, \lambda)}{d\mathbf{m}} = \frac{\partial L(\mathbf{m}, \overline{\mathbf{u}}, \lambda)}{\partial \mathbf{m}} + \frac{\partial L(\mathbf{m}, \overline{\mathbf{u}}, \lambda)}{\partial \mathbf{u}} \frac{\partial \overline{\mathbf{u}}}{\partial \mathbf{m}}. \tag{4}$$

The adjoint state $\overline{\lambda}$ is defined by $\frac{\partial L(\mathbf{m}, \overline{\mathbf{u}}, \overline{\lambda})}{\partial \mathbf{u}} = 0$, which is equivalent to

$$\mathbf{A}^\dagger \overline{\lambda} = \mathbf{R}^\dagger (\mathbf{d} - \mathbf{R}\overline{\mathbf{u}}), \tag{5}$$

where the superscript † represents the conjugate transpose. Therefore, the gradient from eq. (4) is reduced to

$$\nabla_{\mathbf{m}} E = \frac{\partial L(\mathbf{m}, \overline{\mathbf{u}}, \overline{\lambda})}{\partial \mathbf{m}}. \tag{6}$$

It then follows from eq. (2) that the individual components of the gradient vector can be expressed as

$$\nabla_{m_i} E = \Re \langle \frac{\partial \mathbf{A}}{\partial m_i} \overline{\mathbf{u}} \, , \overline{\lambda} \, \rangle. \tag{7}$$

Within a Newton optimization approach, the search direction $\delta \mathbf{m}$ for model update is the solution of

$$\mathbf{H} \, \delta \mathbf{m} = -\nabla_{\mathbf{m}} E, \tag{8}$$

where $\mathbf{H}$ is the Hessian of the objective function. We solve eq. (8) using the l-BFGS method, which uses the information of gradient and model stored from a limited number of previous iterations to approximate the inverse $\mathbf{H}$ (Nocedal and Wright, 2006).

Effective source approach

We consider here an effective source approach for VSP FWI, which attempts to remove the near-surface from the inversion problem (Keating et al., 2021). In this approach, we imagine a line source $\mathbf{f}^*$ at depth z^* such that, when activated, it reproduces the wavefield that would be obtained by propagation through the near-surface. The optimization problem is given by

$$\min_{\mathbf{m}^*, \mathbf{f}^*} E = \frac{1}{2} \|\mathbf{R}^* \mathbf{u}^* - \mathbf{d}^*\|_2^2 \quad \text{subject to} \quad \mathbf{A}^*(\mathbf{m}^*)\mathbf{u}^* = \mathbf{f}^*, \tag{9}$$

where each of the * variables is only allowed to take values at depths below z^*. eq. (9) is effectively the same optimization problem as the conventional one, eq. (1), with the exception that we define the problem on a smaller model domain, and we invert for both an unknown model, $\mathbf{m}^*$, and an unknown source term $\mathbf{f}^*$. In effect, this formulation replaces the problem of characterizing a complex, heterogeneous near surface given a known source

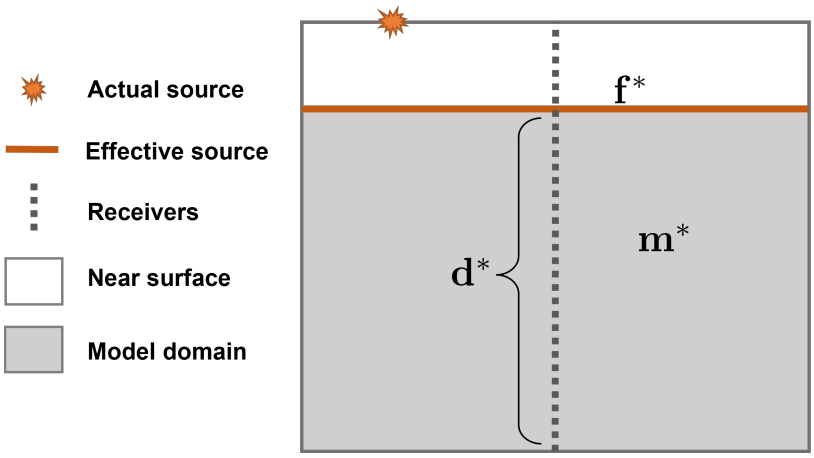

FIG. 1. Schematic depiction of the effective source approach for VSP FWI.

term with the problem of characterizing the wavefield produced by the interaction of the two at a chosen depth. This type of problem is illustrated schematically in Fig. 1.

We can obtain the gradient with respect to the source term $\mathbf{f}^*$ in a way similar to that of the model gradient (eqs 2-6) . The result is

$$\nabla_{f_i} E = -\overline{\lambda}_i, \tag{10}$$

where λ_i is the adjoint wavefield at an effective source location indexed by i. In practice, we initialize $\mathbf{f}^*$ using the modeled wavefield at depth z^* from the initial model, and then simultaneously update $\mathbf{f}^*$ and $\mathbf{m}^*$ using the data recorded at depths below z^*. The choice of z^* requires testing, with the goal being to select the depth that allows the downgoing wavefield complexity to be explained by the effective source.

FWI incorporating DAS data

DAS fiber response is proportional to the strain induced in the fiber by a propagating seismic wavefield. Following the approach of Eaid et al. (2020), we can generate strain data directly in forward modeling to compare with the field DAS data. Here we give a brief description of this approach.

The strain tensor can be defined in Cartesian coordinates as

$$e_{ij} = \frac{1}{2}\left(\frac{\partial u_i}{\partial x_j} + \frac{\partial u_j}{\partial x_i}\right), \quad i,j = 1,2,3. \tag{11}$$

where u_i is the particle displacement in the ith direction. To simulate fiber response, the Cartesian strain tensor must be transformed into the local system describing the fiber, from which the tangential component is extracted. Let the unit vectors $\{\hat{\mathbf{x}}, \hat{\mathbf{y}}, \hat{\mathbf{z}}\}$ denote the inline-crossline-depth Cartesian system and $\{\hat{\mathbf{t}}, \hat{\mathbf{n}}, \hat{\mathbf{b}}\}$ denote the local fiber coordinate defined by the tangent, normal, and binormal directions, we have

$$\mathbf{e}' = \mathbf{P}\mathbf{e}\mathbf{P}^T, \tag{12}$$

where

$$\mathbf{e} = \begin{bmatrix} e_{xx} & e_{xy} & e_{xz} \\ e_{yx} & e_{yy} & e_{yz} \\ e_{zx} & e_{zy} & e_{zz} \end{bmatrix}, \ \mathbf{e}' = \begin{bmatrix} e_{tt} & e_{tn} & e_{tb} \\ e_{nt} & e_{nn} & e_{nb} \\ e_{bt} & e_{bn} & e_{bb} \end{bmatrix}, \tag{13}$$

and $\mathbf{P}$ is the rotation matrix:

$$\mathbf{P} = \begin{bmatrix} \hat{\mathbf{t}} \cdot \hat{\mathbf{x}} & \hat{\mathbf{t}} \cdot \hat{\mathbf{y}} & \hat{\mathbf{t}} \cdot \hat{\mathbf{z}} \\ \hat{\mathbf{n}} \cdot \hat{\mathbf{x}} & \hat{\mathbf{n}} \cdot \hat{\mathbf{y}} & \hat{\mathbf{n}} \cdot \hat{\mathbf{z}} \\ \hat{\mathbf{b}} \cdot \hat{\mathbf{x}} & \hat{\mathbf{b}} \cdot \hat{\mathbf{y}} & \hat{\mathbf{b}} \cdot \hat{\mathbf{z}} \end{bmatrix}. \tag{14}$$

The tangential strain is then

$$\begin{aligned} e_{tt} =& (\hat{\mathbf{t}} \cdot \hat{\mathbf{x}})^2 e_{xx} + (\hat{\mathbf{t}} \cdot \hat{\mathbf{y}})^2 e_{yy} + (\hat{\mathbf{t}} \cdot \hat{\mathbf{z}})^2 e_{zz} \\ &+ 2(\hat{\mathbf{t}} \cdot \hat{\mathbf{x}})(\hat{\mathbf{t}} \cdot \hat{\mathbf{y}}) e_{xy} + 2(\hat{\mathbf{t}} \cdot \hat{\mathbf{x}})(\hat{\mathbf{t}} \cdot \hat{\mathbf{z}}) e_{xz} + 2(\hat{\mathbf{t}} \cdot \hat{\mathbf{y}})(\hat{\mathbf{t}} \cdot \hat{\mathbf{z}}) e_{yz}. \end{aligned} \tag{15}$$

For straight fibers deployed in vertical wells, the fibers have a single, vertical tangent direction, namely $\hat{\mathbf{t}} = \hat{\mathbf{z}}$, resulting in a DAS system sensitive only to the normal strain e_{zz}. In practice, we compute e_{zz} on a grid staggered to that of the displacements, so the strain at each grid cell is approximated as a weighted sum of the neighboring vertical displacements u_z.

FWI incorporating DAS data requires an objective function that compares the observed and modeled fiber strains. The receiver matrix $\mathbf{R}$ in eq. (1) can be understood more generally as an operator that transforms the simulated wavefield into quantities directly comparable to the observed data. Therefore, we can include DAS data in FWI by simply reformulating R. Specifically, we design some rows of R to map the displacement wavefield to the accelerometer positions and the others to compute the tangential strain at channel positions along the fiber. This process of modeling the combined accelerometer and DAS data, $\mathbf{d} = \mathbf{R}\mathbf{u}$, can be expressed as

$$\begin{bmatrix} d_x^1 \\ \vdots \\ d_x^{N_a} \\ d_z^1 \\ \vdots \\ d_z^{N_a} \\ e_{tt}^1 \\ \vdots \\ e_{tt}^{N_d} \end{bmatrix} = \begin{bmatrix} & 1 & & & & & & & \\ \vdots & & & & & & & & \\ & & & & & 1 & & & \\ & & 1 & & & & & & \\ \vdots & & & & & & & & \\ & & & & & & & 1 & \\ & w_1 & w_2 & \dots & w_3 & w_4 & & & \\ \vdots & & & & & & & & \\ & & & & w_1 & w_2 & \dots & w_3 & w_4 \end{bmatrix} \begin{bmatrix} u_x^1 \\ u_z^1 \\ u_x^2 \\ u_z^2 \\ \vdots \\ u_x^N \\ u_z^N \end{bmatrix}, \tag{16}$$

where N is the total number of discrete spatial positions, N_a and N_d are the numbers of accelerometer and DAS sensors, respectively, and w_1, w_2, w_3, w_4 are finite-difference coefficients. This formulation also allows us to include a data weighting matrix in the objective function to control the relative importance of accelerometer data and DAS data in recovering subsurface model.

Bayesian rock physics inversion

Once we have obtained a model of elastic properties $\mathbf{m}$ from seismic data, we then aim to estimate the rock properties $\mathbf{r}$, from $\mathbf{m}$ as the solution of another inverse problem

$$\mathbf{m} = g(\mathbf{r}) + \epsilon, \tag{17}$$

where g is the rock physics model and ϵ is the data error. In this study, the vector $\mathbf{m}$ includes P- and S-wave velocities plus density, and the model variable $\mathbf{r}$ includes porosity and mineral volume fractions. We operate in a Bayesian setting to assess the the conditional probability $P(\mathbf{r}|\mathbf{m})$:

$$P(\mathbf{r}|\mathbf{m}) = \frac{P(\mathbf{r},\mathbf{m})}{P(\mathbf{m})} = \frac{P(\mathbf{m}|\mathbf{r})P(\mathbf{r})}{P(\mathbf{m})}, \tag{18}$$

where $P(\mathbf{r},\mathbf{m})$ is the joint distribution of rock and elastic properties, $P(\mathbf{r})$ is the prior distribution, $P(\mathbf{m}|\mathbf{r})$ is the likelihood function, and $P(\mathbf{m})$ is a normalizing constant. For the prior distribution, we assume a multivariate Gaussian mixture distribution of N_f components:

$$P(\mathbf{r}) = \sum_{k=1}^{N_f} \lambda_k \mathcal{N}(\mathbf{r}; \boldsymbol{\mu}_r^k, \boldsymbol{\Sigma}_r^k), \tag{19}$$

where the distributions $\mathcal{N}(\mathbf{r}; \boldsymbol{\mu}_r^k, \boldsymbol{\Sigma}_r^k)$ represent the k^{th} Gaussian component and the coefficients λ_k are the weights of the linear combination. This assumption allows us to model each litho-fluid class detectable by rock physics analysis as a single component of the Gaussian mixture.

We use the semi-analytical approach of Grana and Rossa (2010) to estimate the conditional probability $P(\mathbf{r}|\mathbf{m})$. First, we generate a set of Monte Carlo samples from the prior distribution $P(\mathbf{r})$ and apply rock physics modeling to obtain the corresponding set of elastic properties $\mathbf{m}$; we then use these samples as a training dataset to estimate the joint distribution of rock and elastic properties assuming a Gaussian mixture distribution:

$$P(\mathbf{r},\mathbf{m}) = \sum_{k=1}^{N_f} \lambda_k \mathcal{N}(\mathbf{y}; \boldsymbol{\mu}_y^k, \boldsymbol{\Sigma}_y^k), \tag{20}$$

where $\mathbf{y} = (\mathbf{r},\mathbf{m})$, and the joint mean and covariance of each component are given by

$$\boldsymbol{\mu}_y^k = \begin{bmatrix} \boldsymbol{\mu}_r^k \\ \boldsymbol{\mu}_m^k \end{bmatrix}, \quad \boldsymbol{\Sigma}_y^k = \begin{bmatrix} \boldsymbol{\Sigma}_{r,r}^k & \boldsymbol{\Sigma}_{r,m}^k \\ \boldsymbol{\Sigma}_{m,r}^k & \boldsymbol{\Sigma}_{m,m}^k \end{bmatrix}. \tag{21}$$

The quantities in eq. (21) can be determined using maximum likelihood estimation (Myung, 2003). As a consequence, the conditional distribution $P(\mathbf{m}|\mathbf{d})$ is a Gaussian mixture:

$$P(\mathbf{r}|\mathbf{m}) = \sum_{k=1}^{N_f} \lambda_k^{'} \mathcal{N}(\mathbf{r}; \boldsymbol{\mu}_{r|m}^k, \boldsymbol{\Sigma}_{r|m}^k), \tag{22}$$

where the conditional weights are given by

$$\lambda_k^{'} = \frac{\lambda_k \mathcal{N}(\mathbf{r}; \boldsymbol{\mu}_{r|m}^k, \boldsymbol{\Sigma}_{r|m}^k)}{\sum_{h=1}^{N_f} \lambda_h \mathcal{N}(\mathbf{r}; \boldsymbol{\mu}_{r|m}^h, \boldsymbol{\Sigma}_{r|m}^h)}, \tag{23}$$

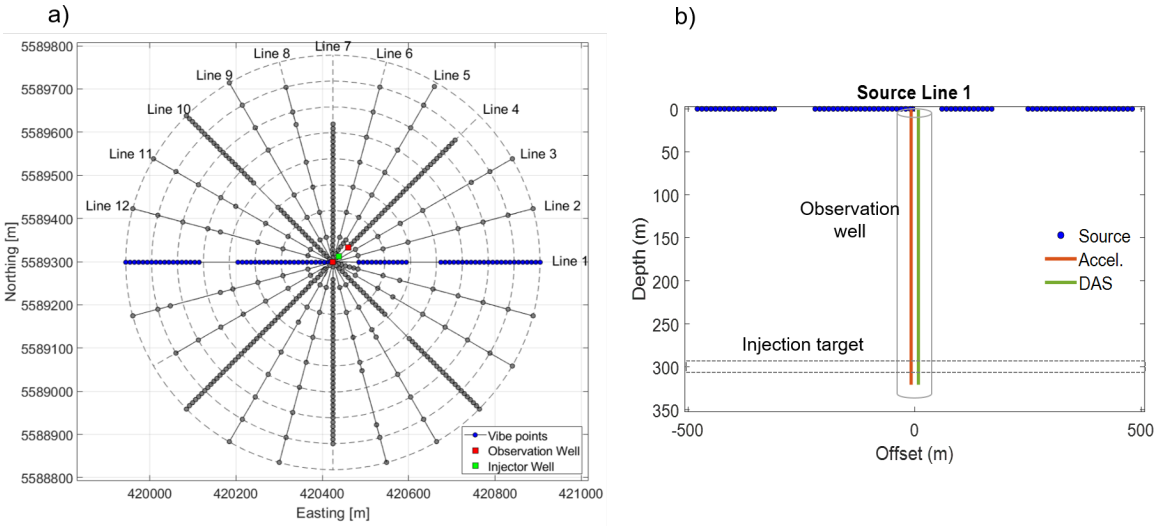

FIG. 2. (a) Shot geometry of the multi-azimuth walk-away VSP experiment at the Newell County Facility. The gray circles represent the locations of vibe points, the green square marks the location of the injection well, and the two red squares mark the locations of the geophysics and geochemistry wells, offset from the injection well by 20 m to south-west and 30 m to north-east, respectively. (b) Section view of the VSP acquisition with respect to source line 1. The horizontal dashed lines delineate the top and bottom of the Basal Belly River Sandstone target reservoir.
.

and the conditional mean and covariance can be analytically derived as

$$\begin{aligned} \boldsymbol{\mu}^k_{r|m} &= \boldsymbol{\mu}^k_r + \boldsymbol{\Sigma}^k_{r,m}(\boldsymbol{\Sigma}^k_{m,m})^{-1}(\mathbf{m} - \boldsymbol{\mu}^k_m) \\ \boldsymbol{\Sigma}^k_{r|m} &= \boldsymbol{\Sigma}^k_{r,r} - \boldsymbol{\Sigma}^k_{r,m}(\boldsymbol{\Sigma}^k_{m,m})^{-1}\boldsymbol{\Sigma}^k_{m,r}. \end{aligned} \tag{24}$$

APPLICATIONS

VSP experiment at CMC Newell County Facility

The Carbon Management Canada's (CMC) Newell County Facility is located 200 km southeast of Calgary, Alberta, Canada. A key goal of this project is the development of technologies for monitoring CO_2 storage (Lawton et al., 2019). The field site houses three wells, including the well being used for CO_2 injection, and two observation wells, colloquially referred to as the geophysics and geochemistry wells. The injection of CO_2 at this site, at a shallow depth of approximately 300 m and at a low flow rate of several tens of tonnes per year (Macquet et al., 2022), is designed to simulate leakage of CO_2 from a deep sequestration site into formations at shallow to intermediate depths. Among the baseline surveys collected in the field, we focus on the multi-azimuth walk-away vertical seismic profile (VSP) dataset acquired in September 2018, which is primarily intended for use in full-waveform inversion (FWI) and modeling studies (Hall et al., 2019).

The 2018 VSP has 12 source lines separated by counter-clockwise fifteen-degree rotations, centered on the geophysics well (Fig. 2a). Source lines 1, 4, 7, and 10 were acquired at a 10 m vibe point spacing and the others were acquired at 60 m spacing. The source was an Inova Univib running a linear sweep from 1-150 Hz over 16 seconds, using 0.2

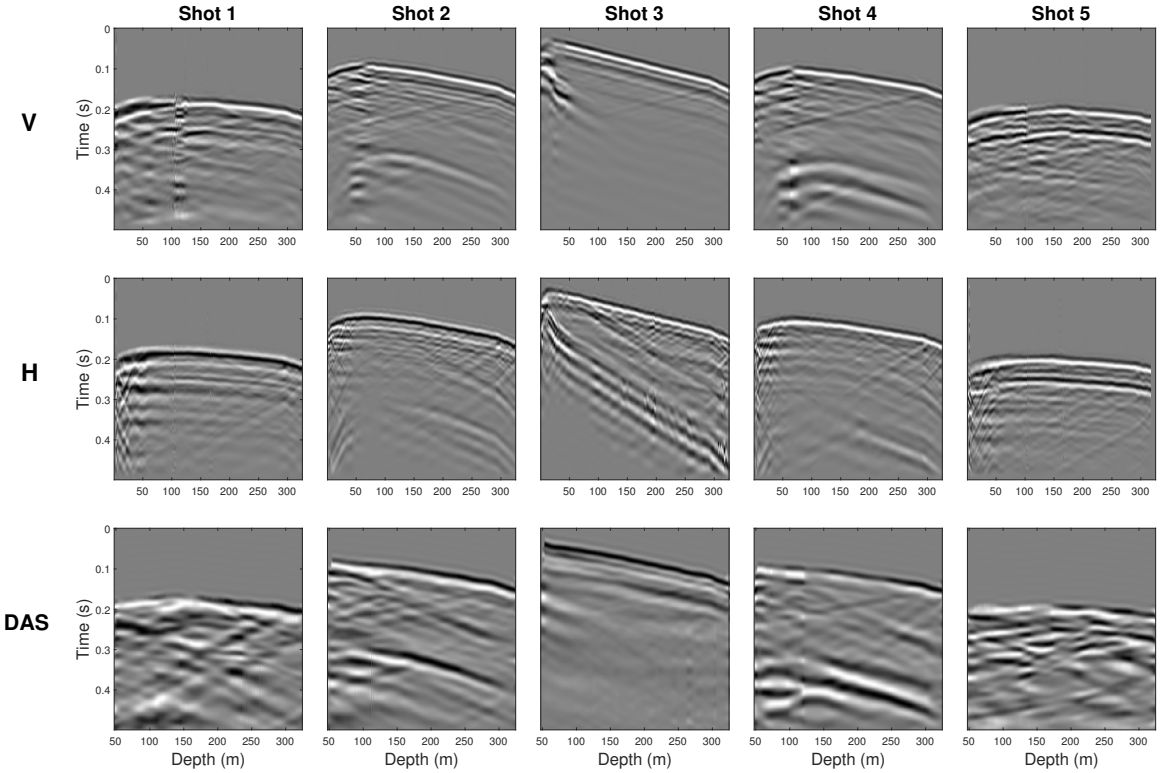

FIG. 3. Processed accelerometer and DAS data for 5 shots on source line 1. Top row: vertical component of acceleration. Middle row: horizontal component of acceleration. Bottom row: DAS-recorded strain. Each column represents the data of a single shot. Shots 1 to 5 correspond to offsets 370 m, 170 m, -20 m, -200 m, and -430 m, respectively.

second half cosine tapers and a 3 second listening time. For this survey, a string of Inova 3C VectorSeis accelerometers were deployed at 1 m spacing from surface to the bottom hole at about 324 m depth. In addition, the geophysics well has a straight DAS fiber and a helical fiber cemented over the entire length of the well, which are part of a 5 km DAS fiber loop permanently buried in the field. Due to computational limitations, we consider 2D FWI, and restrict our analysis to the data generated by source line 1, including both accelerometer and straight DAS fiber measurements (Fig. 2b). This line has 77 shot points. The minimum shot offset from the well was 6 m, and the maximum was 480 m.

Seismic data processing

The seismic data have been carefully processed to be more comparable to simulated data generated by modeling procedures (Eaid et al., 2023). The accelerometer data was processed using a standard workflow for multi-component VSP data, including first break picking, coordinate rotations, trace interpolation and denoising. The DAS data underwent a similar processing workflow, but was simplified due to the single component nature of DAS sensing. However, due to uncertainties in the trace spacing and locations, special attention was directed to depth registration of the DAS data. Fig. 3 plots the processed accelerometer and DAS data for five shot points on source line 1, which represent a portion of the input data for FWI. The result is a high-fidelity two-component accelerometer dataset, whereas the DAS dataset has a relatively low signal-to-noise ratio, especially at far-offset.

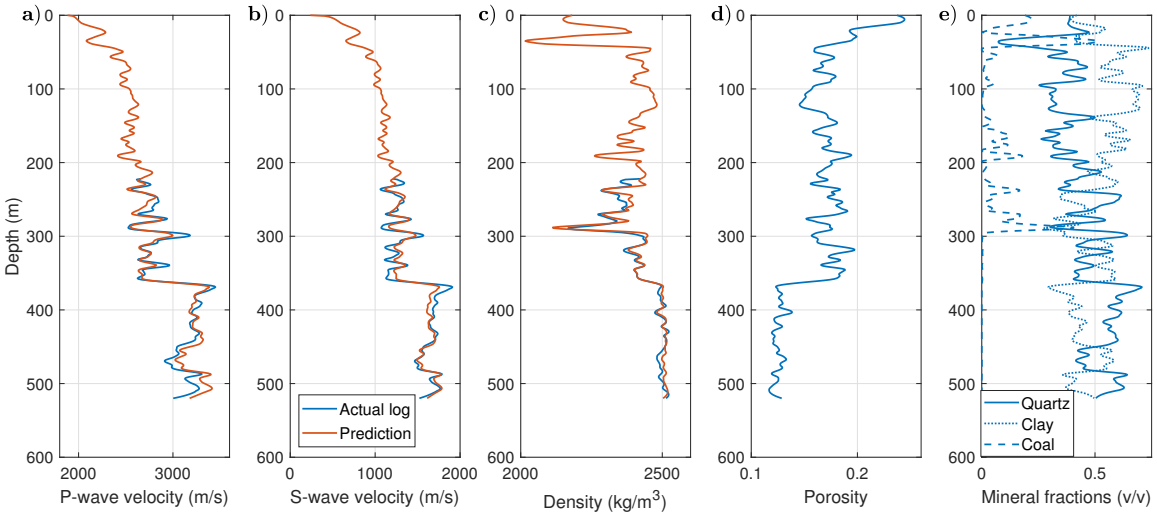

FIG. 4. Well logs (upscaled) of the injection well: (a) P-wave velocity, (b) S-wave velocity, (c) density, (d) total porosity, and (e) the volume fractions of quartz, clay, and coal. Well log data are in blue and rock physics model predictions in orange.

Rock physics analysis of well-log data

A comprehensive log suite was acquired at the injection well (before CO_2 injection), which was drilled to a depth of 550 m to characterize the overburden and the underburden within the field research station. The wireline logs were further interpreted that provides depth profiles of porosity and mineral composition (Fig. 4). The Basal Belly River Sandstone (BBRS) injection zone is at a depth of 296 m below ground surface, and it is a 7-m-thick, fine to medium-grained sandstone at the base of the Foremost Fm. The overlying sealing succession is composed of interbedded mudstone, fine-grained sandstone, and uncleated coals that directly overlies BBRS. Additional seals are provided by a stratigraphically higher coal zone at about 170 m depth. Together, the potential top seal has a combined average thickness of 225 m in the study area (Lawton et al., 2019). Based on the well log data of the range 223-520 m, we have constructed a rock physics model combining the soft-sand model and Gassmann's equations (Mavko et al., 2020) to predict P-wave velocity ($V_{\rm P}$), S-wave velocity ($V_{\rm S}$), and density (ρ) as a function of porosity (ϕ) and mineral volume fractions (Hu et al., 2022):

$$(V_{\rm P}, V_{\rm S}, \rho) = g(\phi, V_{\rm qu}, V_{\rm cl}, V_{\rm co}), \tag{25}$$

where $V_{\rm qu}$, $V_{\rm cl}$, and $V_{\rm co}$ represent the volume fractions of quartz, clay, and coal, respectively, and $V_{\rm qu} + V_{\rm cl} + V_{\rm co} = 1$. Because the in-stu hydrocarbon saturation is sufficiently small (Macquet et al., 2019), the brine saturation was assumed to be 100%. Given its visible fit to the data (Figs 4a-c), the rock physics model was then used to reconstruct the velocity and density logs missed at shallow depths 0-223 m, using the corresponding rock property logs as input. The predictions have a good match with the local geology as well as the first-arrival traveltimes picked on zero-offset seismic data (Kolkman-Quinn, 2022). These increase our confidence in the rock physics model. In the following analysis, the velocity and density logs we refer to contain the model predictions at shallow depths 0-223 m and the original measured data at depths below 223 m.

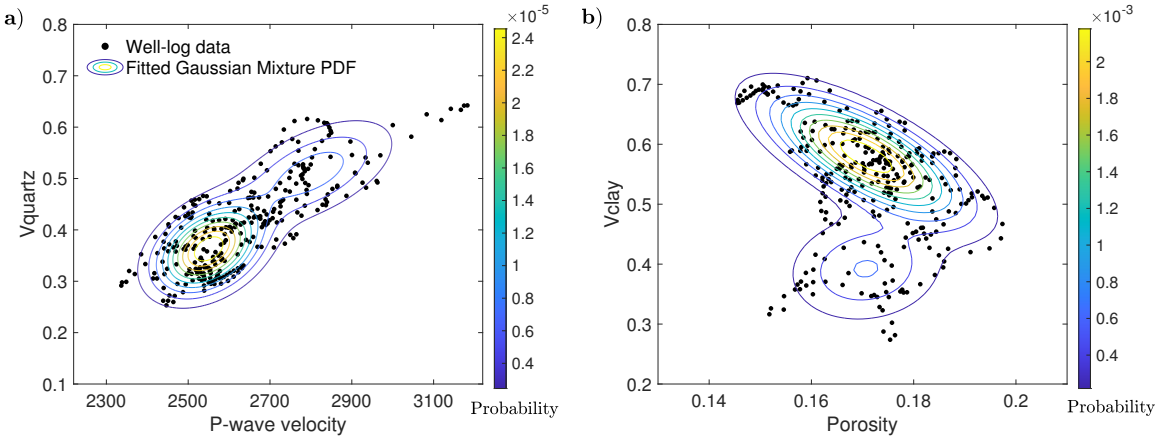

FIG. 5. Bivariate Gaussian mixture probability density function (PDF) estimated from well-log data, in the domain of (a) P-wave velocity and quartz volume, and (b) porosity and clay volume.

To validate our choice of Gaussian mixture models for describing parameter distributions, we draw crossplots of the well-log data in Fig. 5. These data correspond to a depth range of 50 to 350 m, in order to be consistent with the target depth range of subsequent inversions. We assume a joint Gaussian mixture distribution with two components for the elastic and rock properties. For illustration purposes, we only display the bivariate projections in the petro-elastic domain of P-wave velocity and quartz volume, and in the petrophysical domain of porosity and clay volume. The Gaussian mixture model captures the bimodal behavior of the data, with the two components that can be associated with sandy ($V_{\text{clay}} < 0.45$) and shaley ($V_{\text{clay}} > 0.45$) facies.

Elastic FWI results

We consider here a 2D, frequency-domain, three-parameter elastic FWI algorithm. The model we consider is 1000 m wide by 350 m deep (as shown in Fig. 2b), with 2.5 m grid spacing. We use 63 shots from source line 1 that lead to both accelerometer and DAS measurements. Each shot gather is converted from the time domain to the frequency domain through a temporal Fourier transform. The inversion is computed over 7 frequency bands, each containing 6 frequencies that are slightly overlapped, following the multiscale strategy promoted by Keating and Innanen (2019). The minimum frequency we use is 10 Hz, which is found to be the lowest frequency at which the signal-to-noise ratio is acceptable, and the maximum frequency is 25 Hz, which is limited by the computational cost of moving to the smaller finite-difference grid spacing necessary for higher frequencies. We perform 10 iterations of L-BFGS optimization at each frequency band, simultaneously updating the model area below 50 m depth and the effective source at 40 m depth.

The initial models are created by applying Gaussian smoothing to the well logs of V_{P}, V_{S}, and ρ. We run inversions using the accelerometer, DAS, and combined accelerometer-DAS datasets respectively. Due to limited observation aperture, we only demonstrate the recovered models within 200 m offset. In Fig. 6, the results are summarized. The inverted models from either dataset exhibit sufficient updates from the initial one, but have different features. The accelerometer inverted models reveal a reasonable amount of detail in the vicinity of the observation well, but lack lateral continuity, especially for P-wave velocity.

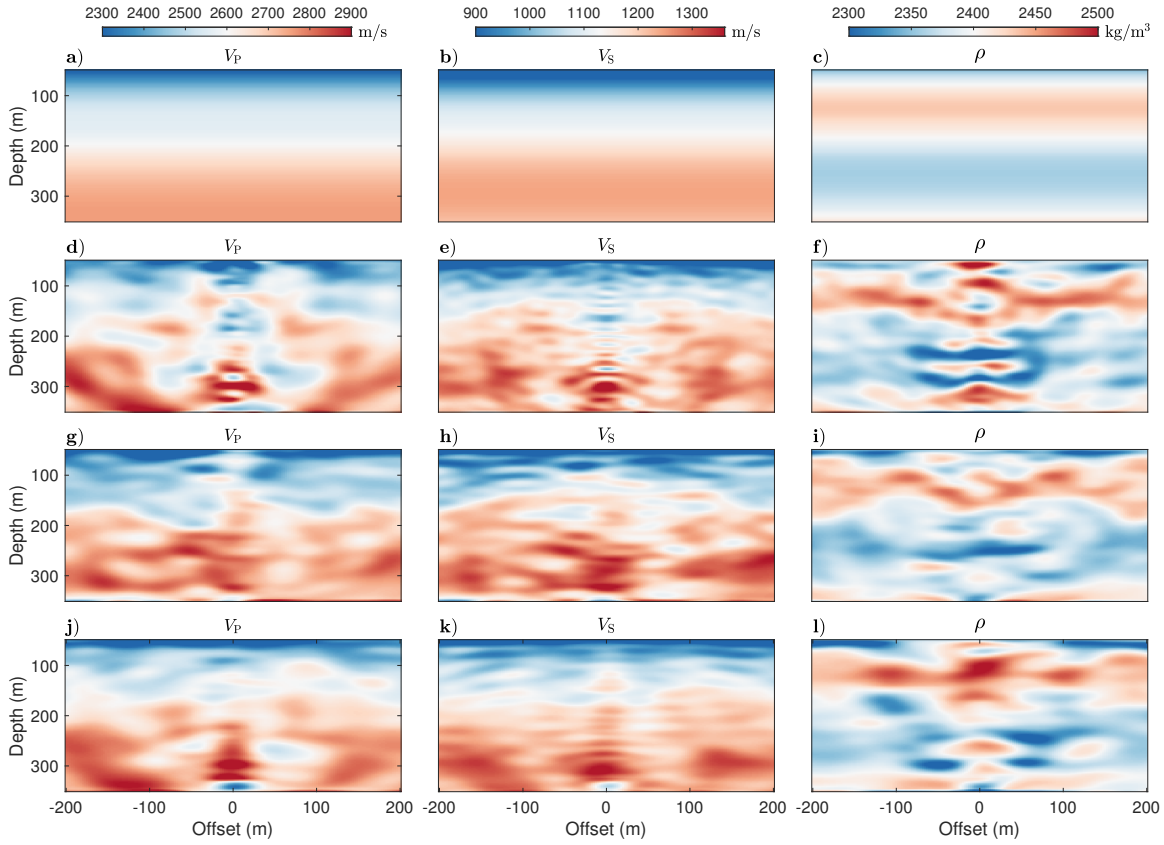

FIG. 6. (a)-(c) Initial models of P-wave velocity, S-wave velocity, and density. (d-f) Inverted models from accelerometer data. (g-i) Inverted models from DAS data. (j-l) Inverted models from combined accelerometer and DAS data.

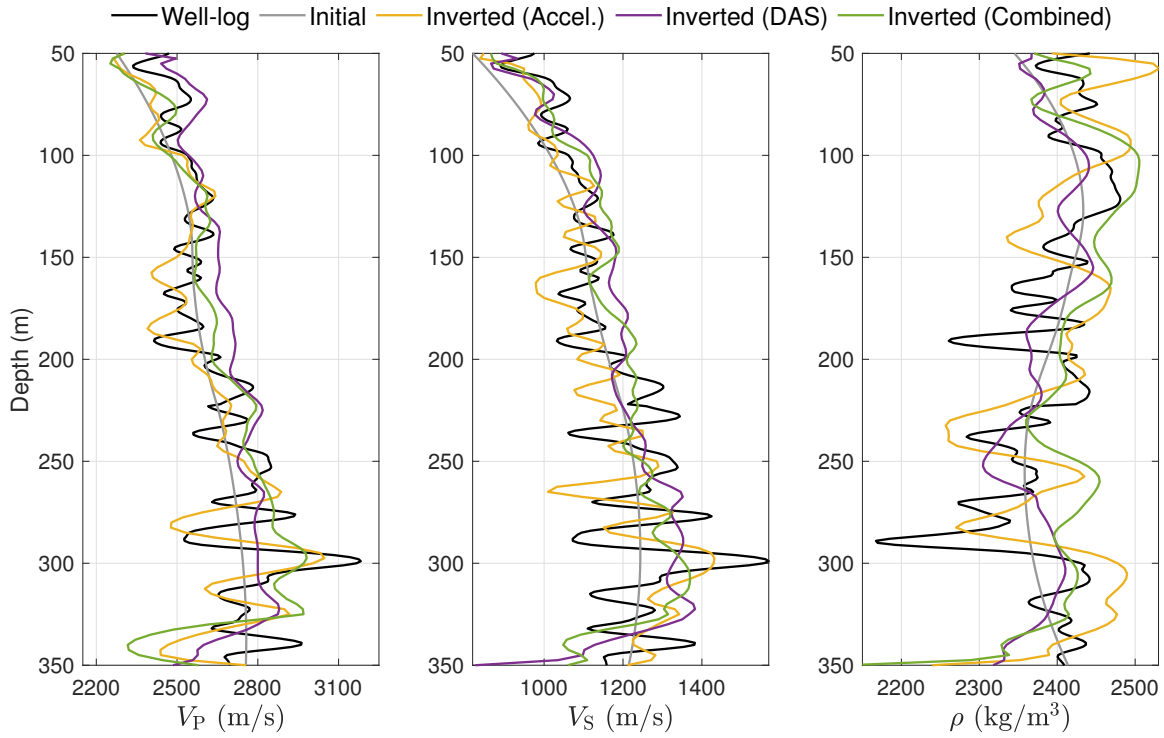

FIG. 7. Comparison of the well logs and the vertical profiles extracted from the initial and inverted models (Figure 6) at offset 20 m.

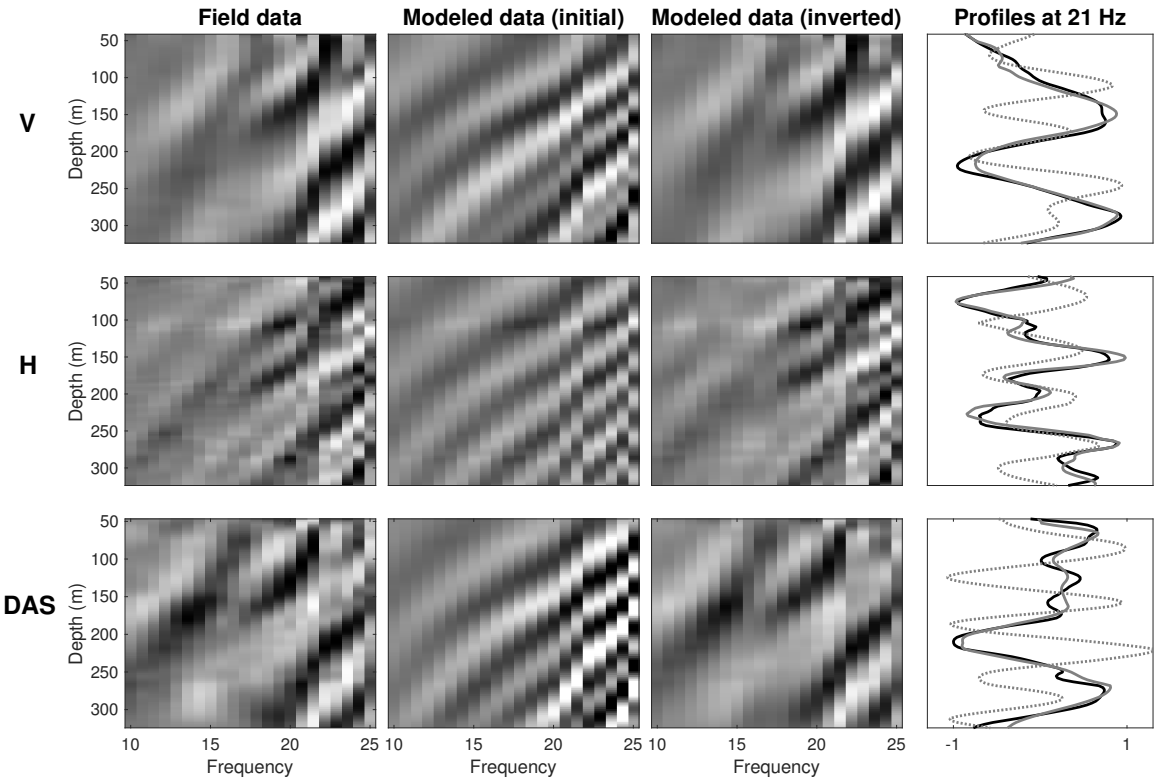

FIG. 8. Real part of frequency domain data for shot at 70 m offset. Top row: vertical component of acceleration. Middle row: horizontal component of acceleration. Bottom row: DAS-recorded strain. Columns from left to right: Field data, modeled data simulated from the initial model, modeled data simulated from the inverted model, and comparison of the 21 Hz field data (solid black line), initial modeled data (dotted gray line), and inverted data (solid gray line).

The DAS model updates are largely layer-like, possibly more geologically meaningful, but have a relatively poor resolution in the near-offset region. The inverted models using both datasets neutralize the model characteristics for each individual data, indicating that our inversion approach is stable. Observation of the model profiles in Fig. 7 suggest that the accelerometer inverted models correlate strongly to the well logs, and capture the large elastic contrast between the caprock and reservoir formations, at approximately 300 m depth. The DAS models correlate relatively poorly with well logs and fail to identify the reservoir of interest. This also brings a great obstacle for us to use the DAS data alone to predict reservoir parameters. We attribute this deficiency to the limited sensitivity of DAS to the wavefield creating strain that is perpendicular to the fiber and the lower signal-to-noise ratio of the DAS data compared to the accelerometer data.

In our FWI procedure, the field data are normalized for each source-receiver pair, to prevent under-emphasizing measurements from deeper areas. In order to compare these re-scaled data to our simulated data in the inversion, the modeled data are also scaled similarly. In Fig. 8, the normalized frequency-domain measured data for the shot at 70 m offset and the corresponding modeled data, simulated from the initial and inverted models, are plotted. As this comparison demonstrates, the data misfit is significantly reduced after inversion. In fact, across all shots, data misfit was reduced by 95% for the accelerometer data and 70% for the DAS data, after each type of data was inverted alone. However, for a

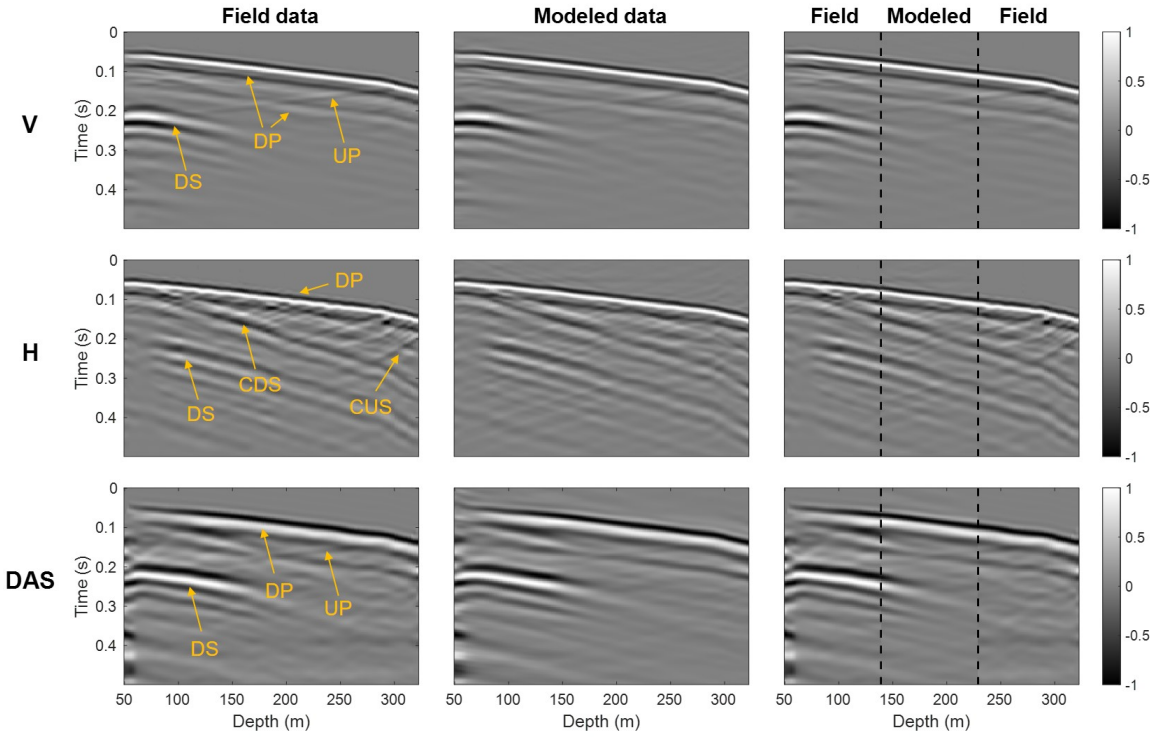

FIG. 9. Time domain data for shot at 70 m offset. Top row: vertical component of acceleration. Middle row: horizontal component of acceleration. Bottom row: DAS-recorded strain. Columns from left to right: Field data, modeled data simulated from the inverted model, and a mixture of field and modeled data. In the panels of field data we marked the different types of waves. DP: downgoing P-waves. DS: downgoing S-waves. UP: upgoing P-waves. CDS: converted downgoing S-waves. CUS: converted upgoing S-waves.

joint inversion of the accelerometer and DAS data, the degree of data fitting will be reduced because each data set will be less emphasized than their individual inversions.

Next, we examine the modeled data in the time domain. To achieve this, we introduce more frequencies to the modeled data, based on the inverted models, and then use inverse Fourier transform to obtain synthetic shot gathers. Fig. 9 illustrates that the modeled data match closely the field data in terms of both amplitude and phase. While the prediction of downgoing wavefield relies on accurate source information and a reasonable initial model, the prediction of upgoing wavefield relies heavily on model updating. The accurate reproduction of both downgoing and upgoing wavefields illustrates that our effective source method is fairly robust.

Rock physics inversion results

In this section, we adopt the FWI models from the accelerometer data to predict the spatial distribution of reservoir properties, given that they outperform the results of either DAS or combined accelerometer-DAS data in identifying the target reservoir. Based on the analysis of well-log data, we define three model unknowns: porosity, quartz volume, and clay volume. The goal is to obtain the posterior probability distribution of these variables conditioned on the FWI models.

We first build a training dataset of 1000 Monte Carlo samples, by sampling from a prior Gaussian mixture distribution, $P(\phi, V_{\rm qu}, V_{\rm cl})$, estimated from the porosity and lithology logs, and applying rock physics model to obtain the corresponding elastic parameters. We then estimate the parameters of the joint distribution, $P(\phi, V_{\rm qu}, V_{\rm cl}, V_{\rm P}, V_{\rm S}, \rho)$, from the training dataset. Finally, we compute the posterior distribution of rock properties conditioned on each set of the elastic parameters from FWI, $P(\phi, V_{\rm qu}, V_{\rm cl} \mid V_{\rm P}, V_{\rm S}, \rho)$, using eqs (22)-(24).

The inversion is first applied at the well location to compare the results with the actual curves of porosity and mineral volumes. In Fig. 10, we observe that the posterior distributions capture the trend of the well logs, with a high fraction of true samples falling inside the 0.95 confidence interval. The maximum a posteriori (MAP) estimate of porosity, although correlates relatively poorly with the actual log, reveals the limited variations of this property across the depth profile, and has a root mean squared error of 0.017. The MAP estimates of mineral volumes are more accurate in deep regions than in shallow ones. For the interval from 280 to 320 m, the correlation between model predictions and well logs is 0.80 for quartz volume and 0.83 for clay volume. We point out that the misclassifications in the posterior probability distributions are due to the lack of accuracy of the FWI results as well as the rock physics model.

Next, we apply the Bayesian approach to the entire FWI model. In Fig. 11, the MAP models of porosity and mineral volumes are plotted. The coal volume is derived from the predicted quartz and clay volumes, as the sum of their volume fractions equals 1 in our formulation. Due to the lack of ground-truth data to compare against, it is difficult for us to verify the distribution of these parameters away from the well. However, we can find several positive features from this result, the most important of which is the successful

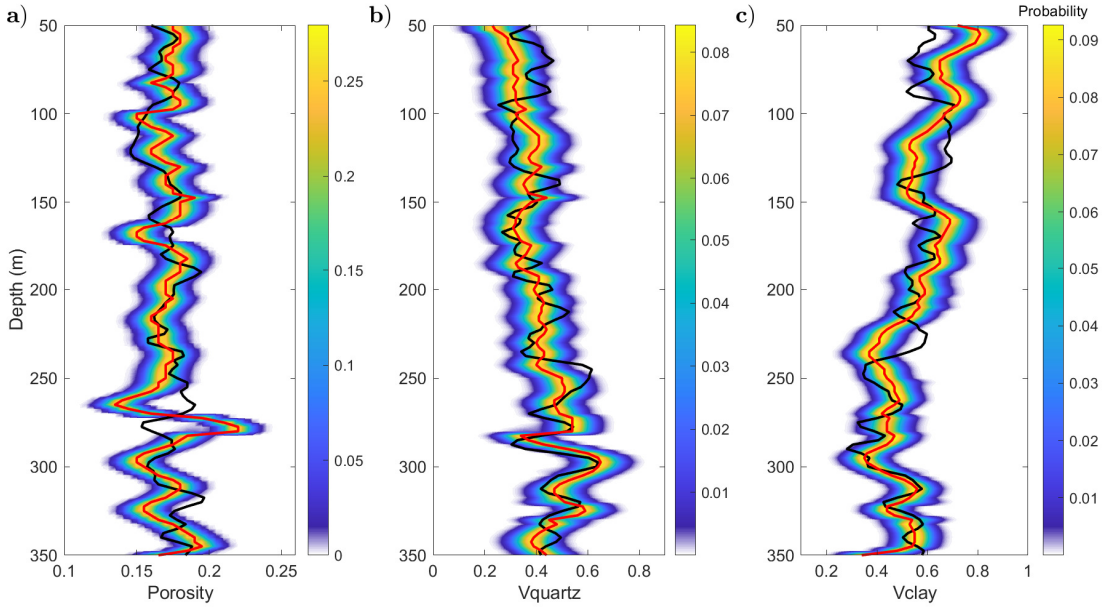

FIG. 10. Posterior distributions of (a) porosity, (b) quartz volume, and (c) clay volume, truncated within the 0.95 confidence interval. The black lines represent the actual well logs and the red lines represent the maximum a posteriori.

identification of the laterally continuous coal zones in the depth range of 200 m to 300 m. These coal zones are estimated to be the main sealing units above the injection area (BBRS). Also, the inverted clay volume is relatively high throughout the model space, which is consistent with the geology in this area, namely, the lithology of the shallow strata is dominated by mudstone and shale-rich sandstone. The inverted porosity values are relatively stable, mainly between 0.15 and 0.2. However, its spatial distribution exhibits a strong degree of blockiness and may contain some artifacts.

DISCUSSION

Although we expect that the combination of DAS and accelerometer data can improve the results of FWI, the premise that this expectation can be realized is that the two types of data are complementary. For example, combining permanently buried DAS fibers in wells with sparsely distributed conventional geophones on the surface can provide the latter with larger observation apertures, more types of seismic waves, denser sampling data, and even lower frequencies. However, when the supplementary effect of DAS is limited, but there are obvious shortcomings, it is worth thinking about whether incorporating DAS data can improve the inversion result. Take the application of this article as an example. The acquisition geometry corresponding to the DAS and accelerometers is the same, the sampling density is the same (1 m), and the lowest acceptable frequency is similar (about 10 Hz), but the DAS can only collect the vertical component of the wavefield, and has a remarkably lower signal-to-noise ratio. Then the help of DAS data is limited, and may even have an adverse impact on the inversion due to data quality. Therefore, we believe it is reasonable to conclude that the accelerometer inversion model is optimal in this case. However, the proposed inversion strategy may play a greater role when DAS data has a clear advantage over conventional geophones, or DAS is the only seismic acquisition mode.

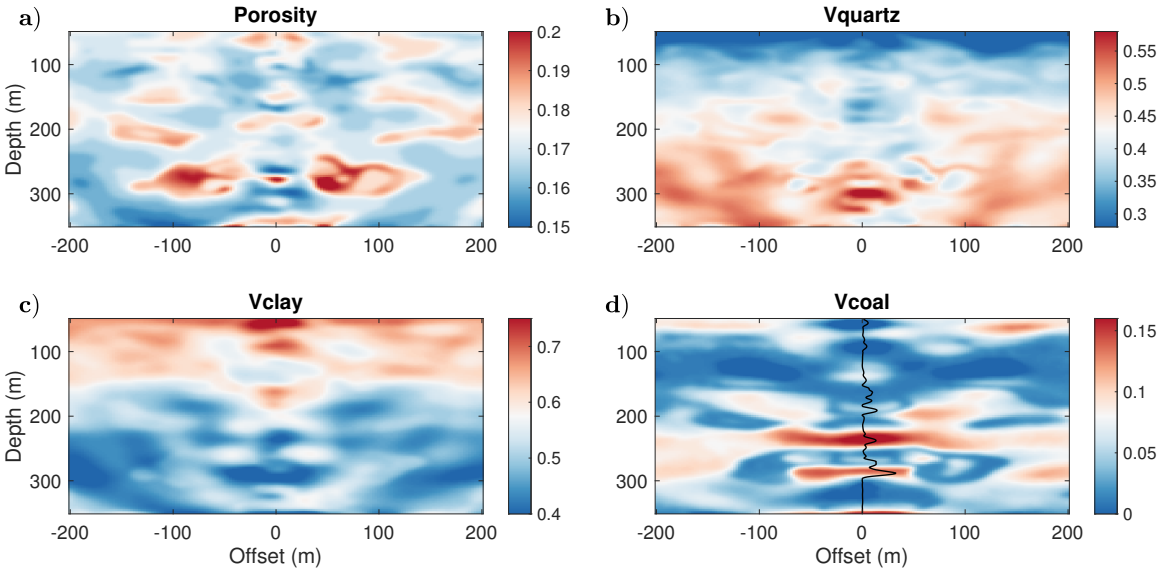

FIG. 11. Inverted models of (a) porosity, (b) quartz volume, (c) clay volume, and (d) coal volume (superimposed the actual log curve).

The proposed effective source method can be regarded as a redatuming method for the VSP system, which takes advantage of the one-way propagation of the wavefield. The reason for us to adopt this approach is that the near-surface complexities bring great difficulties to wavelet estimation and inversions in our study. Although the effective source approach can reduce the near-surface impact, it also brings new challenges, because introducing the wavefield at depth as a variable will increase the non-linearity and non-uniqueness of the inverse problem. So the key is, which one is easier to address, the challenge brought by directly characterizing the near surface with an erroneous wavelet or the challenge brought by the effective source approach. The answer to this question is not unique, depends on the near-surface conditions of the work area, and also depends on the development of inversion strategies for these two types of problems. As far as the field example in this paper is concerned, we found that the effective source method is feasible, and can be viewed as a candidate for solving the near-surface inversion problem.

In seismic reservoir characterization, we focus on porosity, lithology, and fluids. For clastic rocks, porosity, clay volume, and water or gas saturation are the three most common parameters of interest, and are usually treated as unknowns in the inversion. Although some studies have simplified this problem by assuming that the porosity or lithology of the target reservoir interval is known and constant, this treatment is dangerous. There are laboratory studies showing that porosity and clay content are the first and second most important parameters affecting the elastic properties of sand-shale samples. This is why we treat porosity as a model variable, even though its well log exhibits limited variation. In the same way, because the shallow coal seams in the study area greatly reduce the velocity and density of rock, we regard the coal volume as an implicit unknown quantity. One of our simplifications for the baseline study is that the water saturation is 100%. This treatment is fair because previous studies have shown that the in-situ oil and gas saturation is sufficiently low, and also because this parameter is subject to low sensitivity and large uncertainty when it is inverted simultaneously with porosity and lithology parameters. The sensitivity

issues of fluid saturation also exist in the monitor survey. To reduce the uncertainty in the prediction of dynamic reservoir parameters, especially CO_2 saturation and pore pressure, one strategy is to derive porosity and lithology models from baseline data, and then use the results as input for the monitor stage. This makes the baseline prediction of porosity and lithology parameters very important in CO_2 applications, which is also the significance of our research.

CONCLUSION

Carbon capture and storage is an important technology for greenhouse gas mitigation. Time-lapse seismic surveys provide a monitoring mode in which migration and distribution of the injected CO_2 can be tracked. Due to the limited knowledge of rock properties before injection, model predictions are often uncertain and must be updated when new measurements are available. The 2018 CMC VSP survey provided a dataset (accelerometers + DAS) suitable for creating a baseline subsurface model for later time-lapse analysis. In this study, we focus on integrating FWI and rock physics to recover porosity and lithology models from the measured data. To cope with near-surface complications, we used an effective source approach that allows simultaneous updating of wavefield at depth and elastic models. To include DAS data in FWI, we used a modeling strategy that can simulate DAS data that is directly comparable to the field data. To capture the bimodality of rock properties, we used a Gaussian mixture approach to predict the posterior probability distribution of rock physics variables conditioned on FWI results. The inverted elastic models from the accelerometer, DAS, and combined accelerometer-DAS data exhibited different features. In the absence of other verification methods, we judged that the result with the accelerometer data alone is more accurate according to the degree of matching with well-log data. We therefore used this result for the subsequent inversion of reservoir parameters and obtained predictions consistent with the local geology. This study represents an attempt to bring FWI technology into practical use for reservoir characterization.

ACKNOWLEDGMENTS

The sponsors of CREWES are gratefully thanked for continued support. This work was funded by CREWES industrial sponsors, NSERC (Natural Science and Engineering Research Council of Canada) through the grant CRDPJ 543578-19. This work was done in collaboration with the Carbon Management Canada.

REFERENCES

Aki, K., and Richards, P. G., 2002, Quantitative seismology: University Science Books.

Becker, M. W., Ciervo, C., Cole, M., Coleman, T., and Mondanos, M., 2017, Fracture hydromechanical response measured by fiber optic distributed acoustic sensing at millihertz frequencies: Geophysical Research Letters, **44**, No. 14, 7295–7302.

Borisov, D., Gao, F., Williamson, P., and Tromp, J., 2020, Application of 2d full-waveform inversion on exploration land dataapplication of 2d fwi on land data: Geophysics, **85**, No. 2, R75–R86.

Bosch, M., Mukerji, T., and Gonzalez, E. F., 2010, Seismic inversion for reservoir properties combining statistical rock physics and geostatistics: A review: Geophysics, **75**, No. 5, 75A165–75A176.

Brossier, R., Operto, S., and Virieux, J., 2009, Seismic imaging of complex onshore structures by 2D elastic frequency-domain full-waveform inversion: Geophysics, **74**, No. 6, WCC105–WCC118.

Buland, A., and Omre, H., 2003, Bayesian linearized AVO inversion: Geophysics, **68**, No. 1, 185–198.

Byerley, G., Monk, D., Aaron, P., and Yates, M., 2018, Time-lapse seismic monitoring of individual hydraulic frac stages using a downhole das array: The Leading Edge, **37**, No. 11, 802–810.

Colombo, D., Sandoval-Curiel, E., Rovetta, D., and Kontakis, A., 2021, Near-surface full-waveform inversion in a transmission surface-consistent schemefwi in a surface-consistent scheme: Geophysics, **86**, No. 2, U15–U29.

Dokter, E., Köhn, D., Wilken, D., De Nil, D., and Rabbel, W., 2017, Full waveform inversion of sh-and love-wave data in near-surface prospecting: Geophysical Prospecting, **65**, No. S1, 216–236.

Doyen, P., 2007, Seismic reservoir characterization: An earth modelling perspective: EAGE publications.

Dupuy, B., Garambois, S., Asnaashari, A., Balhareth, H. M., Landrø, M., Stovas, A., and Virieux, J., 2016, Estimation of rock physics properties from seismic attributes — Part 2: Applications: Geophysics, **81**, No. 4, M55–M69.

Dupuy, B., Romdhane, A., Eliasson, P., and Yan, H., 2021, Combined geophysical and rock physics workflow for quantitative CO_2 monitoring: International Journal of Greenhouse Gas Control, **106**, 103,217.

Dvorkin, J., Gutierrez, M. A., and Grana, D., 2014, Seismic reflections of rock properties: Cambridge University Press.

Eaid, M. V., Keating, S. D., and Innanen, K. A., 2020, Multiparameter seismic elastic full-waveform inversion with combined geophone and shaped fiber-optic cable data: Geophysics, **85**, No. 6, R537–R552.

Eaid, M. V., Keating, S. D., and Innanen, K. A., 2023, Field assessment of elastic full waveform inversion of combined accelerometer and distributed acoustic sensing data in a vertical seismic profile configuration: Geophysics, accepted for publication.

Egorov, A., Correa, J., Bóna, A., Pevzner, R., Tertyshnikov, K., Glubokovskikh, S., Puzyrev, V., and Gurevich, B., 2018, Elastic full-waveform inversion of vertical seismic profile data acquired with distributed acoustic sensors: Geophysics, **83**, No. 3, R273–R281.

Grana, D., Mukerji, T., and Doyen, P., 2021, Seismic Reservoir Modeling: Theory, Examples, and Algorithms: John Wiley & Sons.

Grana, D., and Rossa, E. D., 2010, Probabilistic petrophysical-properties estimation integrating statistical rock physics with seismic inversion: Geophysics, **75**, No. 3, O21–O37.

Hall, K. W., Bertram, K. L., Bertram, M., Innanen, K., and Lawton, D. C., 2019, Simultaneous accelerometer and optical fibre multi-azimuth walk-away vsp experiment: Newell county, alberta, canada, *in* SEG International Exposition and Annual Meeting, OnePetro.

Harris, K., White, D., Melanson, D., Samson, C., and Daley, T. M., 2016, Feasibility of time-lapse vsp monitoring at the aquistore co2 storage site using a distributed acoustic sensing system: International Journal of Greenhouse Gas Control, **50**, 248–260.

Hu, Q., Grana, D., and Innanen, K. A., 2023, Feasibility of seismic time-lapse monitoring of co2 with rock physics parametrized full waveform inversion: Geophysical Journal International, **233**, No. 1, 402–419.

Hu, Q., Innanen, K., Macquet, M., and Lawton, D., 2022, Rock physics analysis of cami.frs well-log datas: Geoconvention.

Hu, Q., Keating, S., Innanen, K. A., and Chen, H., 2021, Direct updating of rock-physics properties using elastic full-waveform inversion: Geophysics, **86**, No. 3, MR117–MR132.

Jin, G., and Roy, B., 2017, Hydraulic-fracture geometry characterization using low-frequency das signal: The Leading Edge, **36**, No. 12, 975–980.

Keating, S., Eaid, M., and Innanen, K., 2021, Effective sources: removing the near surface from the vsp fwi problem: CREWES Research Reports, **33**.

Keating, S., and Innanen, K. A., 2019, Parameter cross-talk and leakage between spatially-separated unknowns in viscoelastic FWI, 89th Annual International Meeting, SEG, Expanded Abstracts, 1415–1419.

Köhn, D., Wilken, D., De Nil, D., Wunderlich, T., Rabbel, W., Werther, L., Schmidt, J., Zielhofer, C., and Linzen, S., 2019, Comparison of time-domain sh waveform inversion strategies based on sequential low and bandpass filtered data for improved resolution in near-surface prospecting: Journal of Applied Geophysics, **160**, 69–83.

Kolkman-Quinn, B. J., 2022, Time-lapse vsp monitoring of co2 sequestration at the cami field research station: M.Sc. thesis, Science.

Kuvshinov, B., 2016, Interaction of helically wound fibre-optic cables with plane seismic waves: Geophysical Prospecting, **64**, No. 3, 671–688.

Lawton, D. C., Dongas, J., Osadetz, K., Saeedfar, A., and Macquet, M., 2019, Development and analysis of a geostatic model for shallow CO_2 injection at the field research station, southern alberta, canada: Geophysics and Geosequestration. Cambridge University Press, Cambridge, **280**, 296.

Macquet, M., Lawton, D., Osadetz, K., Maidment, G., Bertram, M., Hall, K., Kolkman-Quinn, B., Parra, J. M., Race, F., Savard, G. et al., 2022, Overview of carbon management canada's pilot-scale co2 injection site for developing and testing monitoring technologies for carbon capture and storage, and methane detection: CSEG Recorder, **47**, 1–27.

Macquet, M., Lawton, D. C., Saeedfar, A., and Osadetz, K. G., 2019, A feasibility study for detection thresholds of CO_2 at shallow depths at the cami field research station, newell county, alberta, canada: Petroleum Geoscience, **25**, No. 4, 509–518.

Mallick, S., and Adhikari, S., 2015, Amplitude-variation-with-offset and prestack-waveform inversion: A direct comparison using a real data example from the Rock Springs Uplift, Wyoming, USA: Geophysics, **80**, No. 2, B45–B59.

Mateeva, A., Lopez, J., Potters, H., Mestayer, J., Cox, B., Kiyashchenko, D., Wills, P., Grandi, S., Hornman, K., Kuvshinov, B. et al., 2014, Distributed acoustic sensing for reservoir monitoring with vertical seismic profiling: Geophysical Prospecting, **62**, No. 4-Vertical Seismic Profiling and Microseismicity Frontiers, 679–692.

Mavko, G., Mukerji, T., and Dvorkin, J., 2020, The rock physics handbook: Cambridge university press.

Métivier, L., Brossier, R., Operto, S., and Virieux, J., 2017, Full waveform inversion and the truncated Newton method: SIAM Review, **59**, No. 1, 153–195.

Myung, I. J., 2003, Tutorial on maximum likelihood estimation: Journal of mathematical Psychology, **47**, No. 1, 90–100.

Nocedal, J., and Wright, S. J., 2006, Numerical optimization.

Pan, W., Innanen, K. A., and Geng, Y., 2018, Elastic full-waveform inversion and parametrization analysis applied to walk-away vertical seismic profile data for unconventional (heavy oil) reservoir characterization: Geophysical Journal International, **213**, No. 3, 1934–1968.

Pan, W., Qu, L., Innanen, K. A., Dettmer, J., Macquet, M., Lawton, D., and Wang, Y., 2023, Imaging near-surface s-wave velocity and attenuation models by full-waveform inversion with distributed acoustic sensing-recorded surface waves: Geophysics, **88**, No. 1, R65–R78.

Plessix, R., Milcik, P., Rynja, H., Stopin, A., Matson, K., and Abri, S., 2013, Multiparameter full-waveform inversion: Marine and land examples: The Leading Edge, **32**, No. 9, 1030–1038.

Plessix, R. E., 2006, A review of the adjoint-state method for computing the gradient of a functional with geophysical applications: Geophysical Journal International, **167**, No. 2, 495–503.

Posey Jr, R., Johnson, G., and Vohra, S., 2000, Strain sensing based on coherent rayleigh scattering in an optical fibre: Electronics Letters, **36**, No. 20, 1.

Pratt, R. G., 1990, Frequency-domain elastic wave modeling by finite differences: A tool for crosshole seismic imaging: Geophysics, **55**, No. 5, 626–632.

Queißer, M., and Singh, S. C., 2013, Full waveform inversion in the time lapse mode applied to CO_2 storage at Sleipner: Geophysical prospecting, **61**, No. 3, 537–555.

Stopin, A., Plessix, R.-É., and Al Abri, S., 2014, Multiparameter waveform inversion of a large wide-azimuth low-frequency land data set in oman: Geophysics, **79**, No. 3, WA69–WA77.

Tarantola, A., 1986, A strategy for nonlinear elastic inversion of seismic reflection data: Geophysics, **51**, No. 10, 1893–1903.

Virieux, J., and Operto, S., 2009, An overview of full-waveform inversion in exploration geophysics: Geophysics, **74**, No. 6, WCC1–WCC26.